Available online at www.sciencedirect.com
ScienceDirect
Catalysis Today 131 (2008) 292–304
CATALYSIS TODAY
www.elsevier.com/locate/cattod

Oxyfuel combustion using a catalytic ceramic membrane reactor

Xiaoyao Tan [a], K. Li [a,*], A. Thursfield [b], I.S. Metcalfe [b,**]

[a] Department of Chemical Engineering, Imperial College London, University of London, South Kensington, London SW7 2AZ, UK
[b] School of Chemical Engineering and Advanced Materials, Newcastle University, Newcastle upon Tyne, NE1 7RU, UK

Available online 3 December 2007

Abstract

Membrane catalytic combustion (MCC) is an environmentally friendly technique for heat and power generation from methane. This work demonstrates the performances of a MCC perovskite hollow fibre membrane reactor for the catalytic combustion of methane. The ionic–electronic $La_{0.6}Sr_{0.4}Co_{0.2}Fe_{0.8}O_{3-\alpha}$ (LSCF6428) mixed conductor, in the form of an oxygen-permeable hollow fibre membrane, has been prepared successfully by means of a phase-inversion spinning/sintering technique. For this process polyethersulfone (PESf) was used as a binder, *N*-methyl-2-pyrrollidone (NMP) as solvent and polyvinylpyrrolidone (PVP, K16-18) as an additive. With the prepared LSCF6428 hollow fibre membranes packed with catalyst, hollow fibre membrane reactors (HFMRs) have been assembled to perform the catalytic combustion of methane. A simple mathematical model that combines the local oxygen permeation rate with approximate catalytic reaction kinetics has been developed and can be used to predict the performance of the HFMRs for methane combustion. The effects of operating temperature and methane and air feed flow rates on the performance of the HFMR have been investigated both experimentally and theoretically. Both the methane conversion and oxygen permeation rate can be improved by means of coating platinum on the air side of the hollow fibre membranes.

Keywords: Perovskite membrane; Hollow fibre; Mixed ionic–electronic conductor; Oxygen permeation; Catalytic combustion of methane

1. Introduction

Natural gas containing primarily methane (>95%) is one of the most important energy resources in the world. However, like other fossil fuels, combustion of methane for heat production will inevitably generate not only carbon dioxide but also poisonous gases such as carbon monoxide and oxides of nitrogen. Catalytic combustion is an environmentally friendly technique for heat and power generation from methane, allowing for efficient combustion at methane gas concentrations outside of flammability limits and at temperatures lower than those used in flame combustion without undesired by-products such as unburned hydrocarbons (UHC), carbon monoxide and oxides of nitrogen [1]. Therefore, the development of high performance low-cost methane combustion catalysts has become an active research field in the last few decades [2–11]. At the same time, there is increasing interest in developing methods to capture the carbon dioxide produced in combustion processes as it is believed to be the primary greenhouse gas creating undesired global warming leading to climate change [10,12]. It is possible that carbon dioxide could be reacted with renewably generated hydrogen to produce methanol with carbon dioxide effectively acting as a carrier for the hydrogen fuel. Such capture and recycling strategies are extremely difficult and in many cases may not be feasible because the carbon dioxide-containing stream produced by the traditional combustion process contains a high concentration of nitrogen. The separation of nitrogen and carbon dioxide from such a stream, at the high flow rates required to realise the benefit to the environmental would be extremely expensive.

In order for the MCC process to be attractive for industrial applications, the oxygen permeation rate must be sufficient. This depends not only on the oxygen permeation flux of the membrane but also on the effective membrane area for oxygen permeation. Recently, hollow fibre ceramic membranes with an asymmetric structure have been prepared successfully by means of a phase-inversion spinning/sintering technique [13–16]. Compared to the commonly employed disk-pellet membranes, hollow fibre membranes possess much larger membrane areas per unit volume of reactor. Furthermore, due to

* Corresponding author. Tel.: +44 207 5945676; fax: +44 207 5945629.
** Corresponding author. Tel.: +44 191 2225279; fax: +44 191 2225292.
E-mail addresses: Kang.Li@Imperial.ac.uk (K. Li), I.Metcalfe@newcastle.ac.uk (I.S. Metcalfe).

0920-5861/$ – see front matter © 2007 Elsevier B.V. All rights reserved.
doi:10.1016/j.cattod.2007.10.081

Nomenclature

D_V	effective diffusivity of the oxygen vacancy (cm^2/s)
F_{Air}	air feed flow rate (cm^3(STP)/min)
F_{in}	flow rate of the methane-helium mixture feed (cm^3(STP)/min)
F_{out}	flow rate of the reaction product stream (cm^3(STP)/min)
F_{O_2}	total oxygen permeation rate (cm^3(STP)/min)
J_{O_2}	local oxygen permeation flux (mol/(cm^2 s))
k_1	combustion reaction constant (mol/(g s Pa) (7b))
k_2	combustion reaction constant (mol/(g s $Pa^{1.6}$) (7c))
k_f	forward surface reaction rate constant (cm/($Pa^{0.5}$ s))
k_r	reverse surface reaction rate constant (mol/(cm^2 s))
z	length variable of the hollow fibre membrane (m)
L	length of the hollow fibre membrane (m)
m	number of hollow fibre membranes
N	molar flow rate of gas species (mol/s)
p_a	operating pressure (Pa)
p'_{O_2}	oxygen partial pressures in the shell side (Pa)
p''_{O_2}	oxygen partial pressures in the lumen side (Pa)
r_{CH_r}	combustion rate of methane (mol/(g cat. s))
R	gas constant (8.314 J/(mol K))
R_1, R_2, R_3	individual resistance to oxygen permeation ($Pa^{0.5}$ cm^2 s/mol)
R_{in}	inner radius of hollow fibre (m)
R_m	log-mean radius of hollow fibre (m)
R_o	outer radius of the hollow fibre (m)
R_s	inner radius of the ceramic tube (m)
T	local temperature (K)
t_e	effective thickness of the membrane wall (m)
V_m	conversion of gas volume to moles (22,400 cm^3/mol)
X_{CH_4}	methane conversion (%)
x	component concentration in the product stream, respectively (%)
y_f	methane feed concentration (%)
ρ_b	packing density of catalyst (g/$cm^{3)}$

the asymmetric structure (i.e. a thin separating dense layer integrated with porous layers on one or both sides), the membrane's resistance to oxygen permeation is reduced compared to the symmetric membranes prepared by conventional methods. In addition, the integrated porous layers on one or both sides of the membrane also provide much larger gas-membrane interfaces for oxygen exchange reactions, leading to the enhancement of surface oxygen exchange kinetics and thus improved oxygen permeation rates. The mixed ionic–electronic conducting properties of perovskite membranes provides the membrane with inherent catalytic activity and also avoids the use of electrodes and external circuitry to pump the oxygen from one side to the other as the driving force is the difference in oxygen chemical potential across the membrane. All of these advantages would facilitate perovskite hollow fibre membranes to be used in commercial applications in the foreseeable future.

In this work, the $La_{0.6}Sr_{0.4}Co_{0.2}Fe_{0.8}O_{3-\alpha}$ (LSCF6428) hollow fibre oxygen-permeable membranes have been prepared by the phase-inversion/sintering technique. A hollow fibre membrane reactor (HFMR) has been assembled using the prepared LSCF6428 hollow fibre membranes. The interior of the membranes were packed with a catalyst for methane combustion. A second HFMR module with hollow fibres coated with a layer of platinum on the outside of the membranes has been used and a comparison in performance is made. Post-operation analysis of the membranes indicated that the thermodynamic stress during operation leads to segregation of the constituent perovskite metals but on the time scale of operation this process did not lead to membrane failure or degradation in performance.

2. Experimental

2.1. Materials

Commercially available perovskite $La_{0.6}Sr_{0.4}Co_{0.2}Fe_{0.8}O_{3-\alpha}$ (LSCF6428) powder with a surface area of 9.53 m^2/g and d_{50} = 0.6 μm [purchased from Praxair Surface Technologies, USA] was used as the membrane material. Polyethersulfone, (PESf) [(Radel A-300), Ameco Performance, USA] and *N*-methyl-2-pyrrolidone (NMP) [Synthesis Grade, Merck] were used as the polymer binder and the solvent, respectively. Polyvinylpyrrolidone (PVP, K30) [from Fluka, M_w = 40,000] was used as the additive and also to regulate the viscosity of the starting suspension. A surfactant, Arlacel P-135, was used as the dispersant. The mixture of 50 wt% NMP and deionised water was used as the bore liquid and municipal water used as the external coagulant.

2.2. Preparation of the LSCF6428 hollow fibre membranes and the membrane reactor

LSCF6428 hollow fibre membranes were prepared using a combined phase-inversion/sintering technique, which is described in detail elsewhere [16]. The preparation parameters for producing the LSCF6428 hollow fibre membranes in this work are reported in Table 1. The conditions allowed for gas-tight membranes to be produced.

A catalytic HFMR containing four gas-tight LSCF6428 hollow fibre membranes packed with granular LSCF6428 (30-mesh, ca. 0.6 mm) as the methane combustion catalyst was assembled for the methane combustion experiments. The total amount of catalyst was approximately 0.2 g per hollow fibre, the dimensions of which were typically Ø 0.11 cm× 27 cm. A quartz shell of length 40 cm with internal and external diameters of 2.0 and 2.2 cm, respectively, was used to house the hollow fibres, two pairs of gas inlet/outlets fittings and alumina thermocouple sleeve assembly. These were housed in MACOR end caps (Precision Ceramics, UK) that fitted closely

Table 1
Parameters for preparing LSCF6428 hollow fibre membranes

Starting solution composition (wt%)	Values
LSCF6428 powder	66.27
PESf	6.63
NMP	26.51
PVP	0.5
Dispersant	0.09
Dope temperature (°C)	20
Internal coagulant composition	50% NMP-water solution
Injection rate of internal coagulant (ml min^{-1})	9.0
Nitrogen pressure (atm)	1.0
Air gap (cm)	0
Sintering temperature (°C)	1300
Sintering time (h)	3

Table 2
Characteristic parameters of the hollow fibre membrane reactor

Parameter	Value
Number of fibres, m	4
ID of the shell tube (quartz tube), $2R_s$	2 cm
OD of the hollow fibres, $2R_o$	0.15 cm
ID of the hollow fibres, $2R_{in}$	0.11 cm
Length of the hollow fibres, L	27 cm
Length of the reactor	40 cm
Heated length	13 cm
Size of the LSCF6428 catalyst pellets	30-mesh
Weight of the packed catalyst	0.2 g
Packing length	18 cm
Packing density of catalyst, ρ_b	1.17 g/cm^3

to the inner wall of the shell tubing. The hollow fibres were placed in the module using a pair of MACOR tubes of length 4 cm; each tube is closed at one end with four holes drilled through to accommodate the ends of the hollow fibres. The other end of the MACOR tube is completely open. The open ends of these tubes were attached to the lumen-side gas inlet/outlet housed in the end caps by a length of flexible silicone tubing rated to 238 °C. The sealing was achieved by using a high temperature water-based glass–ceramic sealant (''Light Grade'' Fortafix, UK). A K-type thermocouple which could be moved along the length of the module was inserted inside an alumina sleeve, the tip of which was positioned close to the centre of the hollow fibres allowing the temperature profile to be recorded during operation. Gas flow through the hollow fibres is referred to as being on the ''lumen side'' (''methane side'' and ''reaction side'' are also used) and gas flow outside of the hollow fibres is referred to as being on the ''shell side'' (''air'' and ''air supply'' are also used). The custom made furnace, bore size 3.7 cm (Vecstar Furnaces, UK) had a total length of 15 cm with the heated zone measuring 13 cm in length and a central linear heating zone of 5 cm. The central zone had a drop of 30 °C from its centre point to 2.5 cm either side over the operating temperature range employed. It was assumed that the furnace gave a symmetrical temperature profile. All reactor module temperature changes were at the rate of 3 °C min^{-1} throughout this investigation. The characteristic parameters of the HFMR are summarized in Table 2.

A second HFMR was prepared using four platinum-coated hollow fibre membranes. A platinum resinate (M603B supplied by Metalor, UK) containing 14 wt% of platinum was crudely applied onto the outer surface of the central 5 cm of each hollow fibre using a small fine brush. The membranes were then fired using a programmed temperature ramp of 10 °C min^{-1} to 400 °C, held for 1 h, then 10 °C min^{-1} to 900 °C, held for 1 h, and then 10 °C min^{-1} to 25 °C to remove the organic resin and sinter the platinum metal onto the membrane surface. The average surface loading of the catalytically modified hollow fibres was ca. 3 mg cm^{-2}. Hollow fibre membranes coated with platinum will be referred to hereafter as Pt–HF and uncoated as HF. The procedure for assembling the Pt–HF membranes is as described above. Both modules were loaded with LSCF6428 catalysts on the lumen side.

2.3. Methane combustion experiments

In order to confirm the catalytic activity of the granular LSCF6428 for methane combustion, a pre-experiment was carried out using a fixed bed reactor. It was made of a mullite ceramic tube of length 40 cm and inner and outer diameter of 1 and 1.4 cm, respectively, loaded with 1 g of granular LSCF6428 packed at the centre of the tube. A K-type thermocouple located at the catalyst bed was used to monitor the reaction temperature. The methane supply employed was at a concentration of 9.75%, balance helium (β-standard BOC, UK) and the air supply; 20% oxygen, balance nitrogen (BOC, UK). During operation, the methane and the air were mixed and then co-fed into the reactor tube. The test was performed under different methane and air feed flow rates at 555 °C.

The experimental setup for methane combustion investigations in the HFMR is shown in Fig. 1. The membrane reactor was placed in the above described tubular furnace. During experiments, the temperature profile in the furnace tube was measured using a K type thermocouple by retracting it in either 0.5 or 1 cm steps up to a distance of 10 cm away from the module centre. The temperature at the centre of the reactor was also monitored and used as the temperature of operation for all of the studies reported. The methane was fed into the lumen side, through the catalyst bed while the air supply was introduced cocurrently into the shell side of the reactor. The module gas inlet flow rates were controlled using Chell Hastings and Aalborg mass flow controllers. All gas flows are quoted at standard temperature and pressure (STP). Molar inlet and outlet compositions were obtained by gas chromatography (GC) using a Varian CP-3800 with series-bypass capability. Molecular sieve 5A and Haysep Q columns were used for gas component separation in conjunction with a thermal conductivity detector and helium carrier gas flow of 30 ml min^{-1}. GC calibration was performed using a single gas standard mixture consisting of; 2% hydrogen, 0.5% oxygen, 2% nitrogen, 2% methane, 2% carbon monoxide, 2% carbon dioxide, 2% ethene and 2% ethane (mole fractions with ±2% accuracy). The total analysis time was ten minutes. All gas composition measurements during experiments were made after 30 min following a temperature change or gas supply rate change. At least three analyses were performed for each

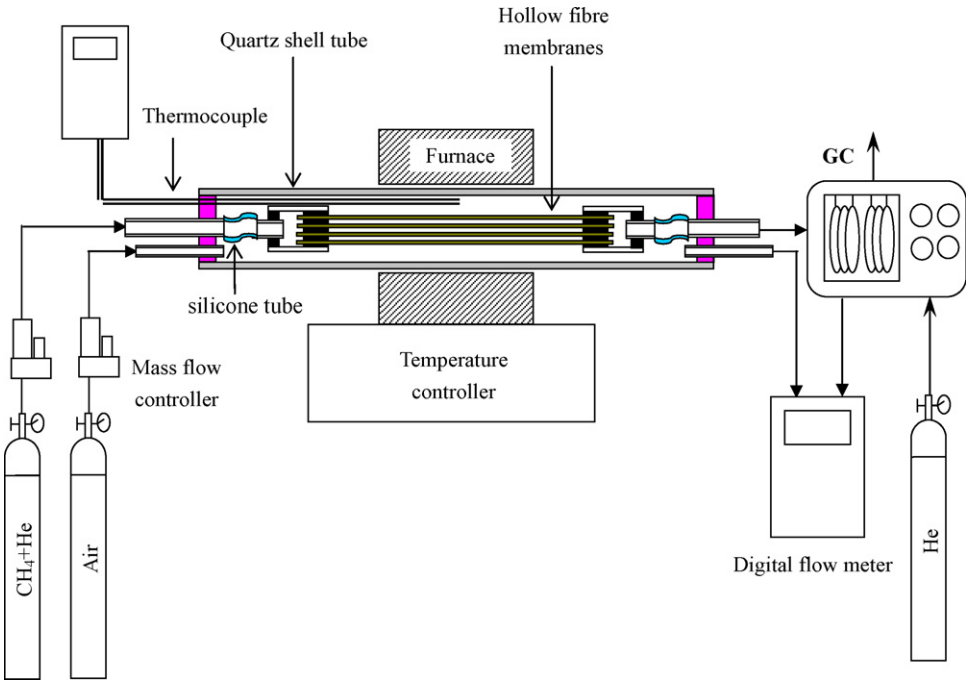

Fig. 1. Experimental setup for the methane combustion investigation.

experimental condition. All experiments were performed at 1 atm on both the shell and the lumen sides. The gas flow rates at the lumen and shell side outlets were independently monitored with a digital flow meter (supplied by Varian Analytical Instruments, UK) accurate to 0.01 ml min^{-1} at the GC gas sampling valve outlet. The integrity of the module seals and membranes were monitored by the nitrogen content in the product stream from the lumen outlet. Throughout the experiments the percentage leakage into the product stream was of the order of 0.4% at the lowest product gas stream flow rate used.

The conversion of methane and selectivity to CO_2 were calculated, respectively, by:

$$X_{CH_4} = \left(1 - \frac{F_{out} x_{CH_4}}{F_{in} y_f}\right) \times 100\% \quad (1)$$

$$S_{CO_2} = \frac{F_{out} x_{CO_2}}{F_{in} y_f - F_{out} x_{CH_4}} \times 100\% \quad (2)$$

where F_{in} and F_{out} are the flow rates of methane feed (methane–helium mixture) and of the product gas stream, respectively; y_f and x are the methane feed mole fraction and the component mole fractions in the product stream, respectively.

The oxygen permeation rate may be determined using the oxygen content of the oxygen-containing species produced during the reaction, i.e. unreacted oxygen permeate, carbon dioxide, carbon monoxide and water. However, as water in the product stream was not measured (it was removed before entering the GC by a cooling trap) the total oxygen permeation rate was estimated based on the stoichiometric coefficients of the reactions to the carbon oxides and C_2 products

$$F_{O_2} = F_{out}(x_{O_2} + 2x_{CO_2} + 1.5x_{CO} + x_{C_2H_4} + 0.5x_{C_2H_6}) \quad (3)$$

where F_{O_2} is the total oxygen permeation rate (cm^3(STP)/min).

Carbon balances across the membrane reactor were also performed. The results varied depending on whether the hollow fibre had a platinum catalyst deposited upon it or not. In general between 83 and 98% of the carbon entering the reactor was accounted for in the product stream. This does indicate that there is significant carbon deposition under some circumstances.

2.4. Microstructure and crystallography

Crystallinity and phase purity was ascertained by powder X-ray diffraction (XRD) using a PANalytical X'Pert Pro diffractometer fitted with a X'Celerator and employing Cu Kα radiation, λ = 1.54180, or Cu Kα1, λ = 1.54059. A nominal step size of 0.033° 2-theta with a step time of 100 s in continuous mode was routinely used. Diffractograms were recorded on ground membrane samples. A Jeol JSM-5300LV-RONTEC EDWIN system was used to perform scanning electron microscopy (SEM) for microstructure characterisation and for standard-less qualitative elemental analysis by energy dispersive X-ray analysis (EDS).

3. Modeling of the membrane reactor

3.1. Oxygen permeation rate through a hollow fibre membrane

Oxygen permeation through the mixed ionic–electronic conducting perovskite membranes is controlled by both the

bulk diffusion of oxygen vacancies in the membrane and the surface oxygen exchange kinetics on either side of the membrane [17,18]. In the absence of mass transfer resistance between gas and the membrane surface, the local oxygen permeation flux through a hollow fibre (or tubular) membrane can be given as [19,20]:

$$J_{O_2} = \frac{k_r[(p'_{O_2})^{0.5} - (p''_{O_2})^{0.5}]}{(R_m/R_{in})(p''_{O_2})^{0.5} + 2t_e((k_f(p'_{O_2})^{0.5}(p''_{O_2})^{0.5})/D_V) + (R_m/R_o)(p'_{O_2})^{0.5}} \quad (4)$$

where the interfacial reactions are described by a simple square root of oxygen partial pressure dependence (i.e. a rate determining step that involves dissociated oxygen). It can be seen that the total permeation resistance is composed of three parts: (1) the exchange reaction at the inner membrane surface (lumen side) ($R_1 = (p''_{O_2})^{0.5}/k_r R_m/R_{in}$), (2) bulk diffusion ($R_2 = 2t_e k_f/k_r(p'_{O_2}p''_{O_2})^{0.5}/D_V$) and (3) the exchange reaction at the outer membrane surface (shell side) ($R_3 = (p'_{O_2})^{0.5}/k_r R_m/R_o$). In the above equations, J_{O_2} is the oxygen permeation molar flow flux, mol/(cm^2 s); R_m is the average radius of the hollow fibre, $R_m = (R_o - R_{in})/\ln(R_o/R_{in})$, in which R_o and R_{in} are the outer and inner radius of the hollow fibre membrane in cm and t_e is the effective thickness of the membrane wall, $t_e = R_o - R_{in}$ for the symmetric membrane. The p'_{O_2} and p''_{O_2} terms are the oxygen partial pressures on the shell side and on the lumen side, respectively, in atm; D_V the diffusion coefficient of oxygen vacancies in the membrane (cm^2/s); k_f (cm/(Pa$^{0.5}$ s)) and k_r (mol/(cm^2 s)) are, respectively, the forward and the reverse reaction rate constants for the surface exchange reaction:

$$\tfrac{1}{2}O_2 + V_O^{\bullet\bullet} \overset{k_f/k_r}{\longleftrightarrow} O_O^x + 2h^\bullet \quad (5)$$

The charged defects are defined using Kröger–Vink notation where O_O^x represents lattice oxygen, $V_O^{\bullet\bullet}$ the oxygen vacancy and $h^\bullet$ the electron hole. Both the diffusion coefficients of the oxygen vacancy and the surface exchange reaction rate constants are functions of temperature but independent of the oxygen partial pressures [18], as listed in Table 3.

3.2. Reaction rate expressions

The reaction kinetics for the combustion catalyst must be known in order to model the HFMR. Although carbon monoxide and C_2 hydrocarbons were produced in the membrane reactor packed with the LSCF6428 catalyst in addition to carbon dioxide, their concentrations were much lower than that of carbon dioxide. Furthermore, they were not observed in the experiments using the fixed bed reactor packed with only the LSCF6428 catalyst. This suggests that LSCF6428 crystallites in non-membrane form at this loading Exhibit 100% selectivity to carbon dioxide and the formation of carbon monoxide and C_2 products resulted from the membrane reactor operation. Therefore for simplification only the complete combustion reaction of methane has been taken into consideration in the following modeling work:

$$CH_4 + 2O_2 \rightarrow CO_2 + 2H_2O\,(g) + \Delta H_c \quad (6)$$

where ΔH_c is the heat of combustion of methane.

Table 3
Oxygen permeation kinetic parameters in the LSCF6428 membrane [18]

Diffusion coefficient of oxygen vacancy (cm^2 s^{-1})	$D_V = 1.58 \times 10^{-2} \exp(-\frac{8852.5}{T})$
Forward reaction rate constant of Eq. (5) (cm atm$^{-0.5}$ s^{-1})	$k_f = 5.90 \times 10^6 \exp(-\frac{27291}{T})$
Reverse reaction rate constant of Eq. (5) (mol cm^{-2} s^{-1})	$k_r = 2.07 \times 10^4 \exp(-\frac{29023}{T})$

Temperatures are in K.

Although no expressions for the kinetic constants are currently available for LSCF6428, the reaction kinetic expressions of methane combustion for LSCF4646 are available in the open literature [2] and are expressed as by:

$$r_{CH_4} = \frac{k_1 p_{CH_4} k_2 (p''_{O_2})^{1.6}}{2k_1 p_{CH_4} + k_2 (p''_{O_2})^{1.6}} \quad (7a)$$

with

$$k_1 = 850 \exp\left(-\frac{1.05 \times 10^5}{RT}\right) \quad (7b)$$

$$k_2 = 350 \exp\left(-\frac{9.2 \times 10^4}{RT}\right) \quad (7c)$$

where r_{CH_4} is the consumption rate of methane, mol/(g cat. s); and k_1 (mol/(g s Pa)) and k_2 (mol/(g s Pa$^{1.6}$))are the reaction constants.

It should be noted that Eq. (7a) may not be the most suitable one for the LSCF6428 catalyst because the actual reaction kinetics depends on the perovskite stoichiometry as well as the structure and particle size of the catalyst. However, the reactor membrane reactor with LSCF6428 catalyst operates at high conversions and we therefore expect models of the reactor to be relatively insensitive to the kinetic expressions used (this idea is tested later in the paper). Therefore, the kinetic expressions of Eq. (7a) have been used as an approximation in the simulation studies in assessing the experimental data.

3.3. Model equations

The model for the HFMR for CCM has been developed based on the experimental setup as described above. That is, the HFMR consists of m LSCF6428 hollow fibre membranes packed with the LSCF6428 granular catalyst. The methane-containing feed and the air stream are cocurrently introduced into the lumen and the shell side, respectively. Fig. 2 illustrates schematically the flow of species in a single packed hollow fibre membrane. The following assumptions have been adopted for the formulation of the governing equations:

(1) Radial concentration gradients either in the catalyst bed are negligible.

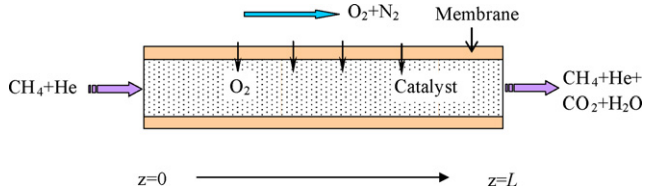

Fig. 2. Schematic of the species flow in a single packed hollow fibre membrane.

(2) Plug flow on both the tube and the shell side. This assumption is valid in the case of turbulent flow, and for large reactor length/tube diameter and tube diameter/particle diameter ratios. Furthermore, the axial dispersion in the catalyst bed is also negligible because of the high flow rate.
(3) The temperature changes due to reaction may be neglected. However, the temperature profile along the hollow fibres as a result of the furnace operation must be taken into consideration.
(4) Furthermore, the intraparticle and interphase mass-transfer resistance can be incorporated into a global reaction kinetics model (pseudohomogeneous reaction).
(5) The catalyst is packed uniformly in the lumen of each fibre, and the packing density is kept constant during the whole experiments.
(6) Ideal gas law is applicable to describe the gas behaviour.
(7) The operation runs at steady state under isobaric conditions.

For each component in the gas streams, the mass conservation equations may be given as follows.

In the shell side,

$$\frac{dN'_{O_2}}{dz} = -2\pi m R_m J_{O_2} \tag{8}$$

In the lumen side,

$$\frac{dN_{CH_4}}{dz} = -r_{CH_4} m\pi R_i^2 \rho_b \tag{9}$$

$$\frac{dN''_{O_2}}{dz} = 2m\pi R_m J_{O_2} - 2r_{CH_4} m\pi R_i^2 \rho_b \tag{10}$$

$$\frac{dN_{CO_2}}{dz} = r_{CH_4} m\pi R_i^2 \rho_b \tag{11}$$

$$\frac{dN_{H_2O}}{dz} = 2r_{CH_4} m\pi R_i^2 \rho_b \tag{12}$$

where N is the molar flow rate of each species in mol/s; m is the number of hollow fibres in the reactor; and ρ_b is the package density of catalyst in g/cm^3.

The boundary conditions are given by:

$$z = 0, [N'_{O_2}, N_{CH_4}, N''_{O_2}, N_{CO_2}, N_{H_2O}] = \left[\frac{0.21F_{Air}}{60V_m}, \frac{F_{in}y_f}{60V_m}, 0, 0, 0\right] \tag{13}$$

where F_{Air} is the air feed flow rate in cm^3/min; and V_m is the conversion ratio of gas volume to moles i.e., V_m = 22,400 cm^3/mol.

The partial pressure of each species may be calculated from the molar gas flow rates and the operating pressure by:

$$p_i = \frac{N_i p_a}{\sum_j N_j}, \quad (i, j = O_2, CH_4, CO_2, H_2O) \tag{14}$$

where p_a is the operating pressure (p_a = 1 atm in this work).

The modeling equations are a group of ordinary differential equations and may be solved numerically using the conventional Runge–Kutta method. The commercial MATLAB software was employed in this work for performing the calculations.

4. Results and discussion

Prior to use samples of freshly fabricated hollow fibre membranes were analysed by XRD, SEM, EDS and tested for gas-tightness. The results indicated that they were comprised of a single perovskite phase, were gas-tight and all surfaces free of foreign particles and could be used for the studies described below. This data is not presented here in order to avoid repetition of similar data reported previously [20,21]. However, a typical XRD powder pattern is presented later in this contribution in order to compare with post-operation membranes (Fig. 9). The micrograph showing the platinum coating on the membrane surface of the Pt–HF module will also be presented later in order to avoid repetition (Fig. 11a).

4.1. Catalytic activity of granular LSCF6428 for methane combustion

The catalytic activity of the granular LSCF6428 catalyst for methane combustion was confirmed using a ceramic fixed bed reactor in which 1 g of LSCF6428 was packed. The test was performed at different methane feed flow rates and a fixed air feed flow rate at 555 °C. The methane feed concentration in all the experiment in this work was kept constant at 9.75%. The experimental results are shown in Fig. 3. It can be seen that the methane can be completely converted if the oxygen supply is sufficient. As the methane feed flow rate increases, more oxygen is converted and the oxygen conversion eventually approaches 100%. Furthermore, no products other than carbon dioxide were observed during the experiments, i.e., the carbon dioxide selectivity is 100%. Therefore we may conclude that the granular LSCF6428 catalyst shows a high catalytic activity to methane combustion. Using the kinetic expression of Eq. (7a), both the methane and oxygen conversions in the fixed reactor were also calculated and plotted on the same figure. As can be seen, experimental data and the calculated values show the same trend. However, at high methane feed flow rate, the calculated oxygen conversion is lower than the experimental data. In order to look at the effect of reaction kinetics, the modeling results with different reaction rates (10 and 100 times higher than the kinetic expression of Eq. (7a)) were also plotted

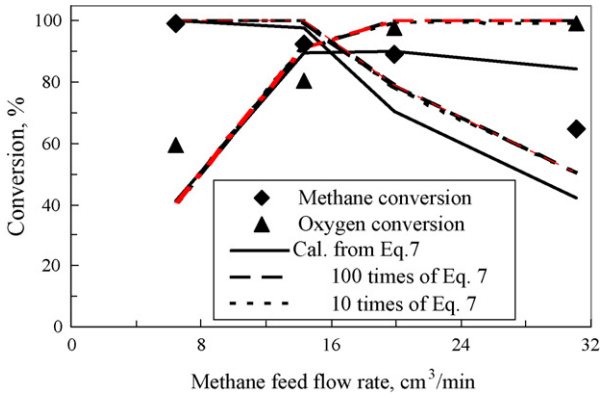

Fig. 3. Methane combustion in the fixed bed reactor (temperature = 555 °C, air feed flow rate = 14.6 cm^3/min).

in the figure. As is expected, the conversion for both methane and oxygen will increase as the reaction rate increases. At high methane feed flow rate, the experimental data are in better agreement with the simulated results using the faster reaction kinetics. However, the difference of the curves using different reaction kinetics is minor, indicating that the methane combustion is relatively insensitive to the combustion kinetics due to the high conversion of the limiting reactant. In view of this, the kinetic expression of Eq. (7a) has been used in the simulation study, even if it is obtained from material of with a slight different stoichiometry.

4.2. Performance of the HF with catalyst

The methane combustion experiments in the HF module were carried out at different temperatures and feed flow rates (both for the methane and the air feed). In order to investigate the effect of a particular operating parameter, all other operating conditions except the specified parameter were kept constant. The experiments described in this work were completed after a period of 96 h. The simulation results using the above mathematical model are also presented along with the experimental data for comparison.

4.2.1. Effect of temperature

Fig. 4 shows the component concentrations in the product stream as a function of temperature. The methane feed was constant at either 10 cm^3/min (Fig. 4a) or 20 cm^3/min (Fig. 4b), and the air flow rate was kept constant at 50 cm^3/min in both cases. As can be seen, apart from the primary product, carbon dioxide, other products such as ethene, ethane (combined and denoted as C_2 in the figures) and carbon monoxide were also produced at low concentrations. The concentration of C_2 hydrocarbons reaches a maximum at 900 °C where the C_2 selectivity is calculated to be 12%. The temperature for the maximum C_2 selectivity increases to 950 °C as the methane feed flow rate is increased to 20 cm^3/min. This phenomenon has also been observed in a LSCF6428 hollow fibre membrane reactor without lumen side packing of a catalyst [22]. However, in the experiments to test the performance of the catalyst using a fixed bed reactor it was found that no C_2 hydrocarbons or

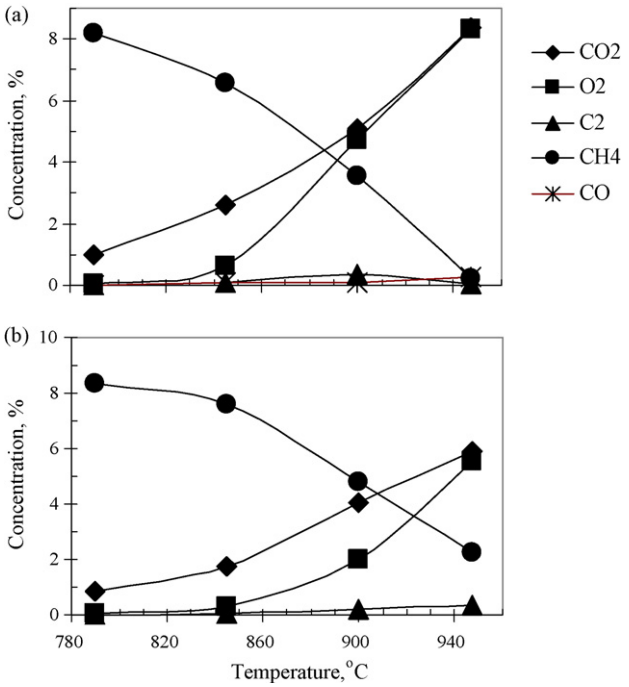

Fig. 4. Compositions of the product stream at different temperatures (a) methane feed = 10 cm^3/min; air feed = 50 cm^3/min, (b) methane feed = 20 cm^3/min; air feed = 50 cm^3/min.

carbon monoxide was formed. It is suggested that the formation of C_2 and carbon monoxide results from the membrane reactor operation, specifically the low LSCF6428 surface area available for catalysis and the consecutive nature of the reaction network (i.e., methane activation resulting in both methyl radical formation with subsequent production of C_2 hydrocarbons and carbon monoxide and hydrogen formation with subsequent total oxidation of C_2 hydrocarbons, hydrogen and carbon monoxide). The oxygen concentration in the product stream was found to increase as the temperature was raised from 790 to 950 °C indicating that the oxygen permeation rate is higher than the oxygen consumption rate due to the reactions.

A comparison between the experimental data and the modeling results is shown in Fig. 5, where both the methane conversion and oxygen permeation rate are plotted against temperature. It can be seen that the mathematical model presented in this work with the reaction kinetics can predict the oxygen permeation rate but fails to accurately predict the experimental methane conversions. This difference may arise from the kinetic expression which may inadequately describe the reaction for the catalyst used. The fact that oxygen permeation rate is predicted accurately indicates that Eq. (4) with the parameters from [18] can be used here in conjunction with an estimate of gas phase partial pressures made by using approximate reaction kinetics. This is the case because, although the approximate kinetics will result in a very large relative error in the estimated partial pressure of the limiting reactant, errors in the estimated partial pressure of the limiting reactant will not affect the prediction of permeation rate from Eq. (4).

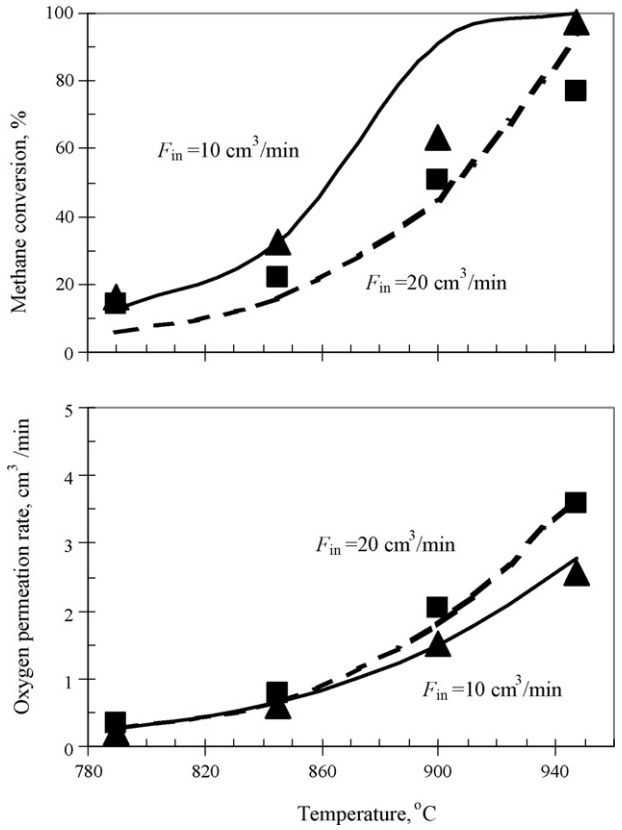

Fig. 5. Comparison of the theoretical results with the experimental data at different temperatures (air feed flow rate = 50 cm^3/min) ((▲ ——), F_{in} = 10 cm^3/min; (– – ■), F_{in} = 20 cm^3/min. the lines represent theoretical results).

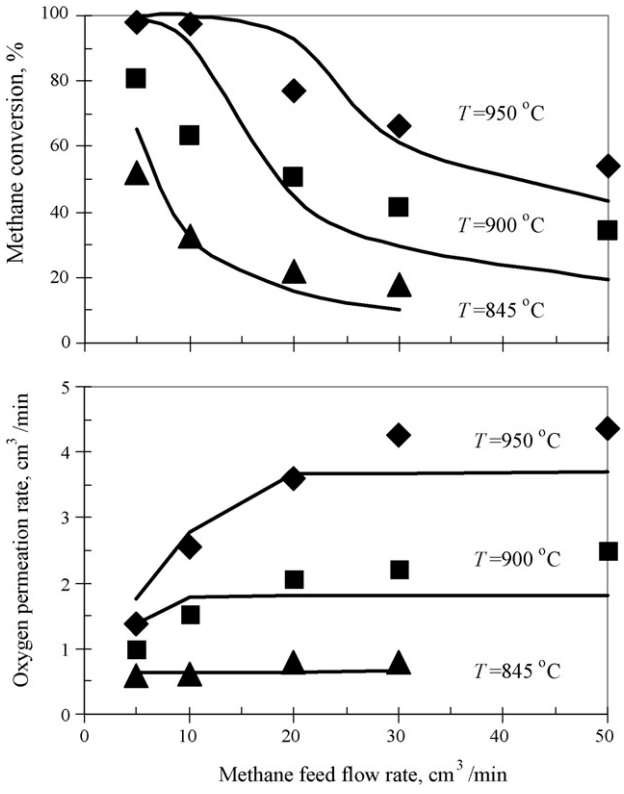

Fig. 6. Effect of methane feed flow rate on the methane conversion and oxygen permeation rate (air feed flow rate = 50 cm^3/min) (the ▲, ■, ◆ symbols represent experimental data and the —— line represents theoretical results).

4.2.2. Effect of methane feed flow rate

Fig. 6 shows the effect of methane feed flow rate on the methane conversion and the oxygen permeation rate at different temperatures while the air feed flow rate is kept constant. As expected it was found that the methane conversion can be increased by increasing the temperature or by decreasing the methane feed flow rate. As the methane feed flow rate is decreased to a certain value the methane conversion can reach 100%, this value depending on the operating temperature. However, the oxygen permeation rate increases with increasing methane feed flow rate but then is almost unchanged when the methane flow rates are very high due to the low methane conversions and hence uniform driving force under these conditions. The modeling results are also plotted and are represented by the solid lines in the figures. It can be seen that the model can adequately predict the trend of the experimental results both for the methane conversion and the oxygen permeation rate.

4.2.3. Effect of air feed flow rate

The effect of air feed flow rate on the methane conversion and oxygen permeation rate as a function of temperature is shown in Fig. 7. The methane feed flow rate was fixed at 20 cm^3/min. As can be seen from Fig. 7a, although the methane conversion can be improved by increasing the air flow rate, the extent dependant on the temperature. At a lower temperature the air feed flow rate has little effect on the methane conversion. At a higher temperature, the methane conversion may be significantly improved as the air flow rate is increased from 10 to 20 cm^3/min; higher air flow rates result in only a small improvement in conversion. The increase in air feed flow rate is consistent with an increased driving force for oxygen permeation. When the air flow rate is increased to higher than 20 cm^3/min the driving force for oxygen permeation does not increase markedly and as a result, both the oxygen permeation rate and the methane conversion are not strongly influenced.

4.3. Enhancement of methane combustion by a platinum coating on the shell side membrane surface—the Pt–HF module

Methane combustion in the HFMR is dependent on the rate of oxygen permeation through the membranes. Therefore application of methods to improve the oxygen permeation rate may assist the methane combustion reaction. In this work, a platinum coating on the hollow fibre membranes' outer surface has been applied to facilitate increased oxygen permeation and tested over a period of 24 h. The results are shown in Fig. 8. It can be seen that the oxygen permeation rate is increased due to the platinum coating and as a result the methane conversion is increased. The coating decreases the outer surface exchange resistance to oxygen permeation, R_3 in Eq. (4), leading to the improvement of oxygen permeation rate and hence methane conversion.

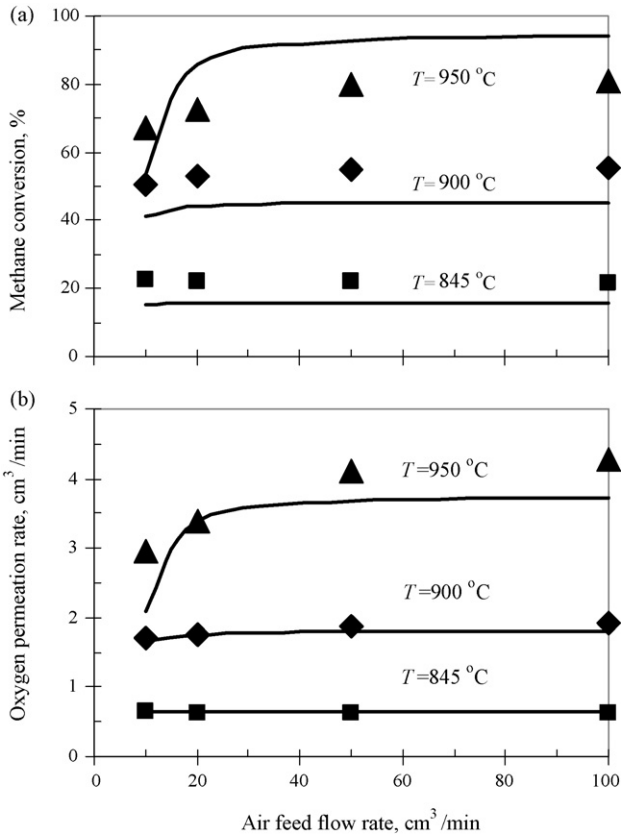

Fig. 7. Effect of air feed flow rate on (a) the methane conversion and (b) oxygen permeation rate (methane feed flow rate = 20 cm^3/min) (the ▲, ■, ◆ symbols represent experimental data and the ━ line represents theoretical results).

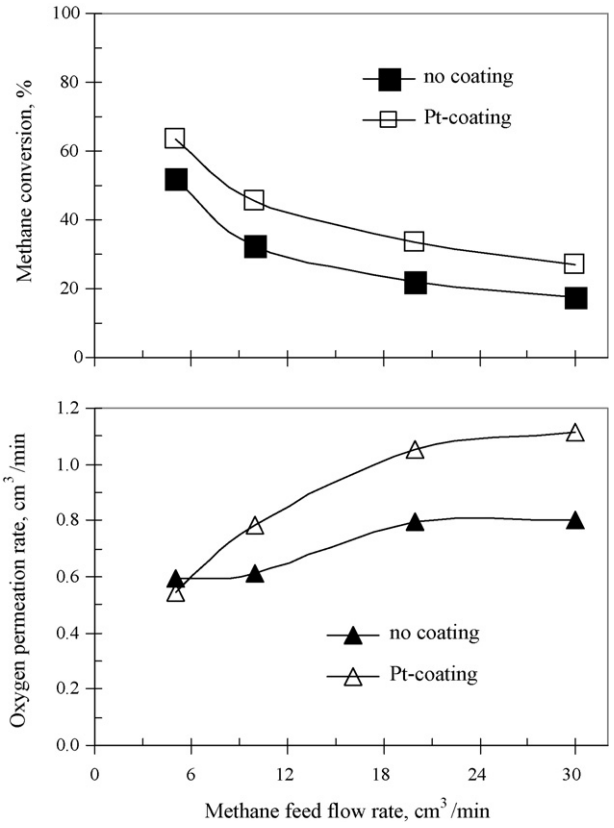

Fig. 8. Effect of platinum coating on the air side of the hollow fibre membranes on methane conversion and oxygen permeation rate (air feed flow rate = 50 cm^3/min) at 845 °C.

4.4. Post-operation analysis of the hollow fibre membranes and catalysts

Following the above-described studies the HF and Pt–HF modules were cooled to room temperature under air and the hollow fibre membranes, the lumen side LSCF6428 catalyst and the platinum coating analysed for possible changes in microstructure and the development of secondary phases. Analysis was performed on membrane samples removed from the centre and ca. 5 cm on either side of the centre point i.e., towards the methane and air gas inlets and outlets. Representative data are presented from the membranes of the HF module only in this section.

Table 4
Post-operation EDS analysis of the shell (air supply) side of the LSCF6428 hollow fibre membranes

Position along the length of the membrane														
Inlet side[a]				Other elements[c]	Centre[b]				Other elements[c]	Outlet side[a]				Other elements[c]
La[c] 30[d]	Sr[c] 20[d]	Co[c] 10[d]	Fe[c] 40[d]	S	La[c] 30[d]	Sr[c] 20[d]	Co[c] 10[d]	Fe[c] 40[d]	S	La[c] 30[d]	Sr[c] 20[d]	Co[c] 10[d]	Fe[c] 40[d]	S
30	20	8	40	2	29	21	9	38	3	28	23	7	38	3
30	20	8	39	3	31	18	9	41	1	26	26	7	35	6
36	7	11	46	0	29	21	8	39	2	27	26	7	36	5
32	13	9	45	0	24	27	9	36	5	34	16	9	41	0
30	20	8	39	2	25	25	8	38	4	29	20	8	40	2
38	15	8	38	1	25	25	8	38	3	45	30	5	24	3
33	12	10	45	0	26	25	9	35	6	44	23	5	24	1
33	15	9	43	0	27	22	9	40	3	48	17	6	26	0
32	16	9	43	0	30	20	9	39	2	45	23	5	24	1
36	16	9	39	0	26	25	8	37	5	25	25	9	38	4

[a] Approximately 5 cm from the centre.
[b] At the centre of the 5 cm linear heated zone.
[c] Rounded to the nearest whole number.
[d] Ideal stoichiometry normalised to 100.

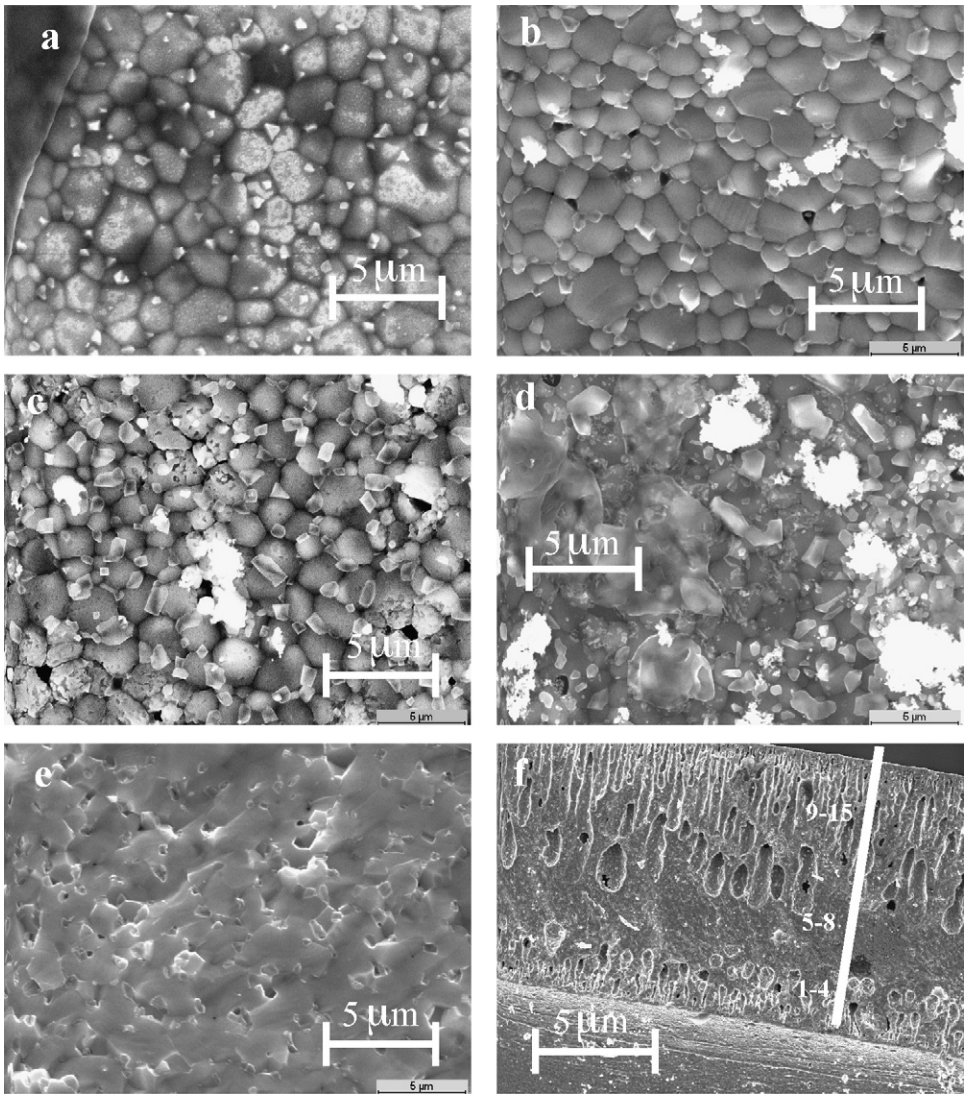

Fig. 9. Post-operation SEM images of (a) the shell side surface which is representative of the entire membrane length (b) the lumen side surface towards the gas inlets (c) the lumen side surface at the centre (d) the lumen side surface towards the gas outlets (e) a representative fracture surface and (f) the location of EDS analysis data points across the membrane fracture surface collated in Table 5 for the three measurement locations.

In Fig. 9 micrograph images of the shell side, lumen side and the bulk (cross-sectional fracture surface of the hollow fibre) membrane surfaces are presented. Fig. 9a shows a representative micrograph of the shell side (air supply side) surface of the centre and towards the gas inlet and outlets. All along the surface there is an even distribution of smaller crystallites decorating the membrane grains. EDS analysis of the surface, ten examples are given in Table 4, performed at well spaced locations, indicated some localised stoichiometry change of the perovskite at the inlet side and centre of the membranes along with the presence of sulfur. Towards the outlet side there is a general enrichment of lanthanum and strontium, again with the presence of sulfur. The lumen side (methane supply/reaction side) shows more variation in microstructure on going from the inlet, (Fig. 9b) to the centre (Fig. 9c) and towards the outlet (Fig. 9d). There is an increase of the presence of smaller crystallites decorating the surface along with agglomerates of much finer crystallites that appear much brighter than the other features. EDS analysis on the lumen surface (Table 5), as for the shell side, indicates that the most significant changes in the LSCF6428 stoichiometry occurred towards the gas outlet side of the membranes in conjunction with more sulfur contamination compared to that observed on the synthetic air exposed shell side surface. Here, we observe significant segregation of lanthanum relative to cobalt. The fracture surface at the three analysis positions did not reveal any microstructural changes and appeared identical to the pre-operation condition; a typical image is presented in Fig. 9e for completeness. EDS analysis across the fracture surface was done in 15 locations; from ‘‘1’’ at the edge of the lumen side through to ‘‘15’’ at the edge of the shell side as depicted in Fig. 9f. Analysis locations 1–4 span the porous lumen side region (ca. 50 μm); locations 5–8 span the inner dense region (ca. 50 μm) and locations 9–15 span the porous outer shell side region (ca. 100 μm). The results of the analysis for the inlet side, the centre and outlet side regions of the membrane are presented in Table 6. Similarly to the EDS

Table 5
Post-operation EDS analysis of the lumen (methane supply) side of the LSCF6428 hollow fibre membranes

Position along the length of the membrane														
Inlet side[a]				Other elements[c]	Centre[b]				Other elements[c]	Outlet side[a]				Other elements[c]
La^c 30^d	Sr^c 20^d	Co^c 10^d	Fe^c 40^d	S	La^c 30^d	Sr^c 20^d	Co^c 10^d	Fe^c 40^d	S	La^c 30^d	Sr^c 20^d	Co^c 10^d	Fe^c 40^d	S
30	20	8	40	2	30	19	8	39	3	41	31	6	20	8
30	20	8	39	3	28	22	8	37	5	41	18	7	22	7
36	7	11	46	0	28	21	8	38	5	45	9	7	25	1
32	13	9	45	0	30	20	8	39	4	32	7	4	16	13
30	20	8	39	2	29	21	7	38	5	41	14	6	22	6
38	15	8	39	1	30	19	9	39	3	44	15	5	24	2
33	12	10	44	0	28	21	8	40	5	38	19	4	21	7
33	15	9	43	0	30	20	8	38	4	42	23	5	22	3
32	16	9	43	0	27	23	8	36	5	43	24	7	22	4
36	16	9	39	0	30	20	8	40	3	41	31	6	20	8

[a] Approximately 5 cm from the centre.
[b] At the centre of the 5 cm linear heated zone.
[c] Rounded to the nearest whole number.
[d] Ideal stoichiometry normalised to 100.

data presented above, we observe that the most significant stoichiometry changes of the membrane occurred towards the gas outlet side with respect to strontium and in particular, lanthanum, with sulfur also detected throughout the membranes. It appears that the increasing presence of the crystallite ''debris'' in the direction of the methane flow at the lumen side corresponds to increasing segregation of lanthanum and to a lesser degree, strontium. This effect may arise from the heating of the methane–oxygen permeate-product gas mixture as it travels along the hollow fibre, becoming more reactive with itself and the wall of the membrane. In addition, the gas flow may physically move light crystallites along its path over a period of time adding to the build up of debris towards the gas outlet. This effect was not observed on the shell side surface possibly because the oxygen does not actually chemically react with the perovskite as can methane (or its products following reaction) although the even sprinkling of much smaller crystallites on the surface indicate that oxygen exposure at high temperatures can change the surface microstructure even after relatively short periods of time. The nature of the EDS analysis did not facilitate identification of the various crystallites found on the shell and lumen side membrane surfaces but

Table 6
Post-operation EDS analysis of the bulk of the LSCF6428 hollow fibre membranes along a vector from the lumen (methane) to the shell (air) side

Location	Inlet side[a]				Other elements[c]	Centre[b]				Other elements[c]	Outlet side[a]				Other elements[c]
	La^c 30^d	Sr^c 20^d	Co^c 10^d	Fe^c 40^d	S	La^c 30^d	Sr^c 20^d	Co^c 10^d	Fe^c 40^d	S	La^c 30^d	Sr^c 20^d	Co^c 10^d	Fe^c 40^d	S
1[e]	29	23	8	38	3	25	26	7	32	10	26	25	7	37	6
2[e]	31	18	8	42	0	27	22	8	38	5	30	22	8	39	2
3[e]	23	18	27	33	1	27	22	8	38	5	24	23	11	33	8
4[e]	28	20	16	37	0	26	24	7	38	5	25	26	6	34	8
5[e]	33	16	9	42	0	26	25	8	35	7	25	23	11	36	5
6[f]	26	23	11	36	4	25	24	9	35	7	41	25	5	22	3
7[f]	32	17	9	42	0	25	24	9	37	6	43	26	5	23	3
8[f]	31	46	4	18	1	23	25	11	34	8	41	27	6	22	4
9[f]	32	19	8	41	1	27	23	8	36	6	34	22	5	21	1
10[g]	29	22	9	38	2	26	23	11	37	3	45	16	5	24	0
11[g]	29	22	9	38	2	38	16	8	37	0	42	27	5	23	3
12[g]	29	21	11	39	2	29	21	10	39	1	37	20	5	22	1
13[g]	29	24	8	39	1	25	7	7	35	7	39	22	7	22	2
14[g]	29	25	8	38	1	22	28	7	35	7	51	20	6	25	1
15[g]	26	26	9	37	2	24	28	6	31	10	24	27	7	33	8

[a] Approximately 5 cm from the centre.
[b] At the centre of the 5 cm linear heated zone.
[c] Rounded to the nearest whole number.
[d] Ideal stoichiometry normalised to 100.
[e] Porosity region at the lumen side.
[f] Along the dense central region.
[g] Along the porosity region on the shell side.

the high sulfur content along with the evidence for lanthanum and strontium segregation indicates the possibility of sulfate formation. Accounts of sulfate formation [23–25], segregation of the constituent membrane elements [23–25] leading to the formation of new phases [24–27], in studies similar to those presented in this contribution where total oxidation, partial oxidation or oxidative coupling of methane have been investigated, are not uncommon in the open literature. The origin of the sulfur contamination has been proposed to be sulfur dioxide in the atmosphere and in the methane (or helium) gas supply. In this work another possible source is the polyethersulfone used to form the hollow fibres prior to sintering and would explain the presence of sulfur in the bulk; however EDS on fresh membrane samples did not indicate the presence of sulfur before use. No sulfur was detected in the bulk of the Pt–HF membranes which were operated for only 24 h, indicating that time of operation may play a role.

In Fig. 10 XRD powder patterns of a sample of fresh membrane and used membrane samples removed from the same EDS analysis locations described above are presented for comparison. The LSCF6428 membranes have retained their perovskite structure but additional low intensity peaks are also observed which are more apparent for the used LSCF6428 lumen side catalyst sample removed from the centre of a hollow fibre membrane. Additional peaks to the perovskite phase (indicated by "P") indicated the presence of $SrSO_4$ (PDF

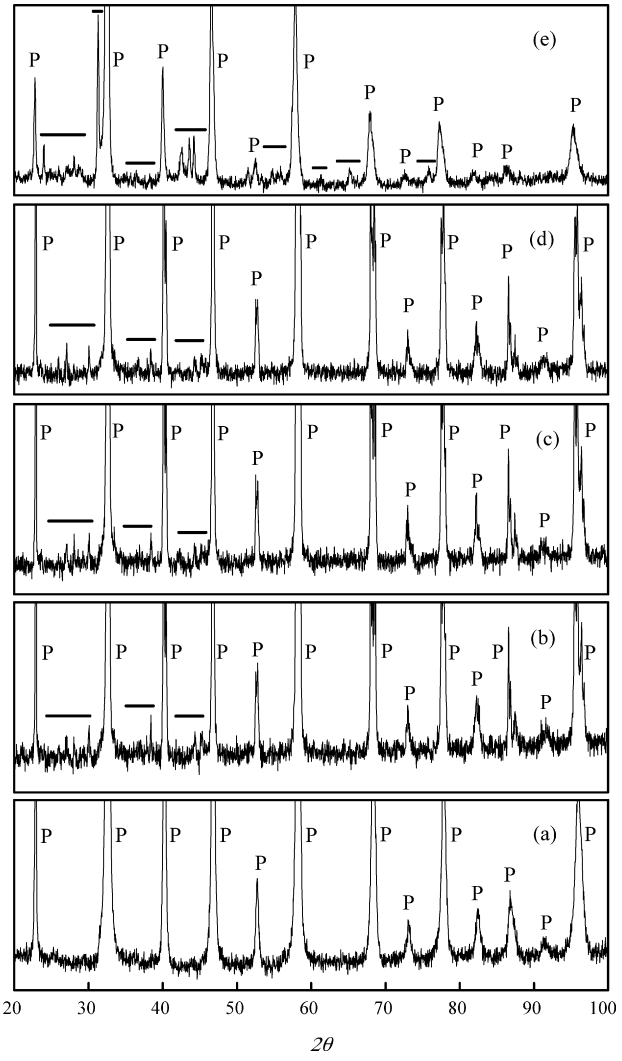

Fig. 10. XRD powder patterns of (a) fresh unused hollow fibre membrane (b) post-operation membrane towards the gas inlets side (c) post-operation membrane at the centre (d) post-operation membrane towards the gas outlest side and (e) post-operation lumen side LSCF6428 catalyst sample from the centre. The peaks associated with the LSCF6428 perovskite are indicated with a P and ▬ represents locations of additional peaks to the pre-operation perovskite reflections.

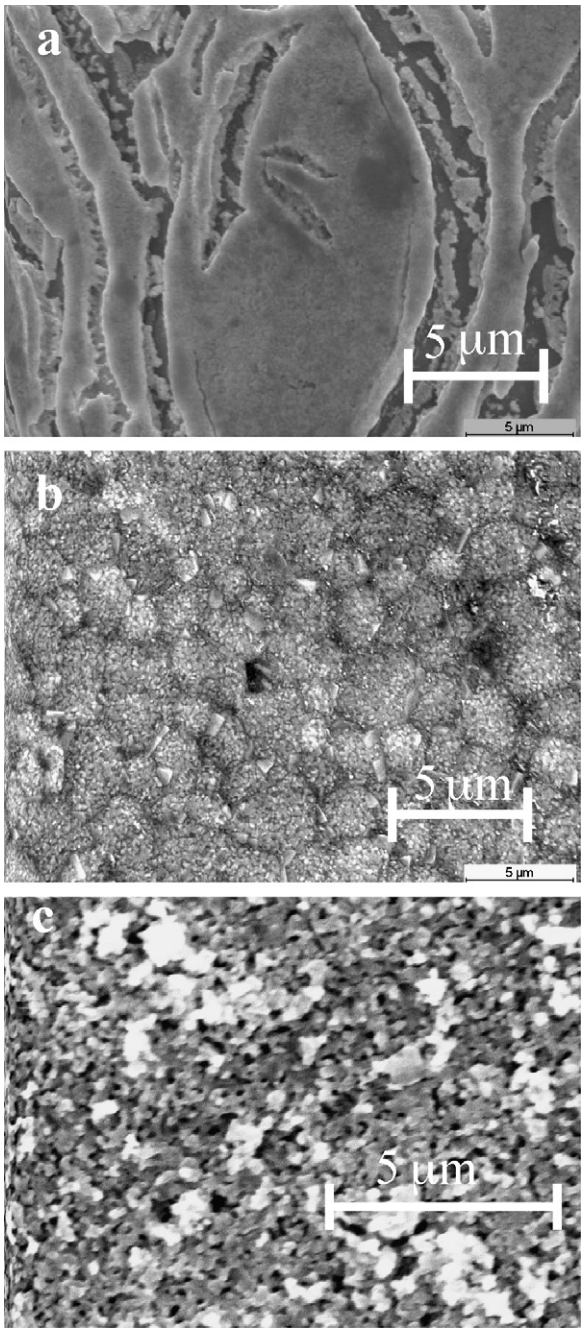

Fig. 11. Post-operation SEM images of (a) platinum coating on a Pt–HF hollow fibre membrane (b) uncoated membrane surface of a Pt–HF hollow fibre membrane and (c) LSCF6428 catalyst surface.

reference code 00-005-0593) in the membrane samples and the $LaSrFeO_4$ phase (PDF reference code 01-071-1745) in the lumen side loaded LSCF6428 catalyst.

The thermodynamic stress caused by the presence of oxygen and methane on either side of dense perovskite membranes at high temperatures may cause kinetic demixing over time leading to segregation and secondary phase formation. The SEM and EDS data and point to this being the case. However, on the timescale of the experiments described in this work, this degradation did not manifest itself by e.g., a drop in oxygen permeation or decreasing methane conversion. The membranes remained intact with only a small nitrogen leak from the shell side through to the lumen side methane stream.

A sample of the LSCF6428 catalyst from the centre section of the HF module membranes and a sample of the platinum-coated membranes of the Pt–HF module were analysed after operation. The platinum coating was found to remain unchanged after 24 h of operation (Fig. 11a). Between the brocken sections of the platinum coating the membrane grains were heavily pitted and decorated in small crystallites (Fig. 11b), this micrograph is particularly blurred and may be indicative of a layer covering by another phase. EDS strongly indicated the presence of sulfur and segregation of strontium between the platinum catalyst areas.

The surface of the centre LSCF6428 catalysts grains is blurred showing extensive break up to give a porous appearance (Fig. 11c) with only very small traces of sulfur indicated by EDS (data not given). The lack of sulfur on the catalyst surface is puzzling as it possessed a higher surface area than the membrane lumen surface for any sulfur dioxide in the methane to react with the perovskite, and so deposition of sulfur might have been expected to occur as found on the membrane surfaces. The surface porosity may be due to the formation of $LaSrFeO_4$ from the LSCF6428 starting material as indicated by the XRD powder pattern although EDS data did not indicate a predominance of this stoichiometry at the surface. The formation of this phase did not change the activity or selectivity of the catalyst with respect to complete methane combustion.

5. Conclusions

$La_{0.6}Sr_{0.4}Co_{0.2}Fe_{0.8}O_{3-\alpha}$ (LSCF6428) hollow fibre membranes have been prepared successfully by the phase-inversion spinning/sintering technique. The prepared hollow fibre membranes packed with catalysts have been assembled in reactors which are suitable for the catalytic combustion of methane. Due to the membrane reactor operation, C_2 hydrocarbons (ethane and ethene) and carbon monoxide may be produced in addition to the main product i.e., carbon dioxide. During operation both the methane and the air feed flow rates should be chosen carefully in order to control the product composition and to improve combustion efficiency. By means of platinum coating on the membrane outer surface, both the oxygen permeation rate and the methane conversion may be improved. A simple model which combines the oxygen permeation rate with the catalytic reactions has been developed and adequately predicts the performance of the hollow fibre membrane reactor.

Post-operation analysis of the membranes revealed changes in the perovskite metal cation stoichiometry and microstructure together with contamination with sulfur which may have its origins in the methane gas supply and sulfur dioxide in the atmosphere. On the timescale of the studies the degradation did not adversely affect performance. The lumen side LSCF6428 catalyst developed a second phase which did not adversely affect the methane combustion process.

Acknowledgements

The authors gratefully acknowledge the research funding provided by EPSRC in the United Kingdom (grant Numbers: GR/S12203 and GR/S12197). ISM acknowledges the support of the Centre for Process Innovation, Wilton, UK.

References

[1] S. Cimino, A. Di Benedetto, R. Pirone, G. Russo, Catal. Today 83 (2003) 33.
[2] D. Klvana, J. Vaillancourt, J. Kirchnerova, J. Chaouki, Appl. Catal. A 109 (1994) 181.
[3] G. Saracco, G. Scibilia, A. Iannibello, G. Baldi, Appl. Catal. B 8 (1996) 229.
[4] G. Saracco, F. Geobaldo, G. Baldi, Appl. Catal. B 20 (1999) 277.
[5] D. Klvana, J. Kirchnerová, J. Chaouki, J. Delval, W. Yaïci, Catal. Today 47 (1999) 115.
[6] T.J. Toops, A.B. Walters, M.A. Vannice, Appl. Catal. A 233 (2002) 125.
[7] R. Kikuchi, S. Maedab, K. Sasaki, S. Wennerström, K. Eguchi, Appl. Catal. A 232 (2002) 23.
[8] P.T. Wierzchowski, L.W. Zatorski, Appl. Catal. B 44 (2003) 53.
[9] S. Ordóñez, P. Hurtado, H. Sastre, F.V. Díez, Appl. Catal. A 259 (2004) 41–48.
[10] M. Ishida, H. Jin, T. Okamoto, Energy Fuels 10 (1996) 958.
[11] H.W.J.P. Neomagus, G. Saracco, H.F.W. Wessel, G.F. Versteeg, Chem. Eng. J. 77 (2000) 165.
[12] R. Bredesen, K. Jordal, O. Bolland, Chem. Eng. Process. 43 (2004) 1129.
[13] X.Y. Tan, S. Liu, K. Li, J. Membr. Sci. 188 (2001) 87.
[14] S. Liu, X.Y. Tan, K. Li, R. Hughes, J. Membr. Sci. 193 (2001) 249.
[15] J. Luyten, A. Buekenhoudt, W. Adriansens, J. Cooymans, H. Weyten, F. Servaes, R. Leysen, Solid State Ionics 135 (2000) 637.
[16] X.Y. Tan, Y.T. Liu, K. Li, Ind. Eng. Chem. Res. 44 (2005) 61.
[17] D. Stefan, J.V. Herle, J. Eur. Ceram. Soc. 24 (2004) 1319.
[18] S.J. Xu, W.J. Thomson, Chem. Eng. Sci. 54 (1999) 3839.
[19] X.Y. Tan, K. Li, AIChE J. 48 (7) (2002) 1469.
[20] X.Y. Tan, Y.T. Liu, K. Li, AIChE J 51 (7) (2005) 1991.
[21] A. Thursfield, I.S. Metcalfe, J. Solid State Electrochem. 10 (2006) 604.
[22] X.Y. Tan, K. Li, Ind. Eng. Chem. Res. 45 (2006) 142.
[23] J.E. ten Elshof, H.J.M. Bouwmeester, H. Verweij, Appl. Catal. A 130 (1995) 195.
[24] R.H.E. van Doorn, H.J.M. Bouwmeester, A.J. Burggraaf, Solid State Ionics 111 (1998) 263.
[25] W. Jin, S. Li, P. Huang, N. Xu, J. Shi, Y.S. Lin, J. Membr. Sci. 166 (2000) 13.
[26] S. Lee, S.K. Woo, K.S. Lee, D.K. Kim, Desalination 193 (2006) 236.
[27] F. Iguchi, N. Sata, H. Yugami, H. Takamura, Solid State Ionics 177 (26–32) (2006) 2281.